Lithographically Defined Micropost Arrays for Programmable Actuation and Interfacial Hydrodynamics

Jacob T. Brooks,* Jeremy Cribb, Michael R. Falvo, and Richard Superfine*

ABSTRACT: Magnetically actuating surface-attached post (ASAP) arrays have great potential in microfluidic flow control, including mixing and pumping. Both passive (nonactuating) and active (actuating) micropillar arrays can also be used to control pressure-driven flow and the motion of microscopic particles carried by the fluid through microfluidic channels. Molding techniques are popular for generating these microstructures. However, fabricating high aspect ratio elastomeric microstructures over large surface areas suffers from practical problems such as damage incurred in the demolding process. Here, we report on a fabrication protocol that generates ASAP with an aspect ratio as high as 23:1 and a cross-sectional area less than 1 μm^2 using straightforward photolithography processes. We generated 50 unique ASAP arrays, each occupying an area of 1 mm^2 on a silicon mold; these arrays have varied cross-sectional shape and size, aspect ratio, and spacings between neighboring posts. Our protocol also controls the level of magnetic material in the ASAP tips with a centrifugation step. Using a herringbone pattern ASAP array, we have demonstrated control over the relative phase of actuation between neighboring posts. Such ASAP serve as an experimental platform to test current models predicting that reciprocal actuators in close proximity can successfully drive flow in a low Reynolds (Re) number environment.

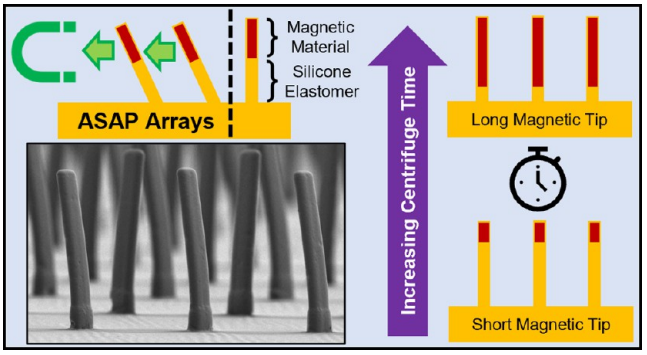

KEYWORDS: *high aspect ratio, micropillars, magnetic nanoparticles, microfabrication, low Reynolds number, microactuators, magnetic actuation*

INTRODUCTION

Cilia-driven fluid transport and mixing phenomena in biological systems have inspired the fabrication of synthetic micropillars for research and industrial fluid manipulation applications.[1−6] Pumping, mixing, and particle sorting in low Reynolds number (Re) environments present technical challenges requiring attention to both cutting edge fabrication techniques as well as the latest understanding of fluid physics in the Stokes (low Re) regime. Synthetic micropillar arrays have also been used as a platform for studying cellular structure and forces[7,8] and have even been used for light manipulation[9] and synthetic adhesive development.[10] In microfluidic applications, passive micropillars are used for particle sorting in microfluidic channels based on principles of deterministic lateral displacement (DLD) and collisions with obstacles in the channel.[11−14] Though the interplay between pillar design parameters has been explored in theoretical and experimental models, the transitional regime between open flow and obstructed flow in a microfluidic device at the border of the area populated by the micropillars remains largely unexplored. To effectively test models of transport and mixing, it is imperative to have a design-based and robust fabrication process. We have achieved this by combining projection lithography to precisely define post cross-section and array geometry, centrifugal deposition to control magnetic loading, and wet release to generate high aspect ratio soft structures.

The fabrication process must be reproducible while permitting nuanced control over all design parameters. Molding methods using photolithography techniques that provide control over nearly every aspect of post design have been demonstrated for fabricating soft microscopic structures.[1,2,9,15−25] Our fabrication protocol uses a projection photolithography process, starting with a photomask printed from a computer-assisted design (CAD) layout. This permits rapid processing of large array areas (100 mm^2 and larger) patterned with millions of high aspect ratio pillars with cross-sections at the micron and submicron scale. Downstream processing steps allow control over the final height and mechanical and magnetic properties of these micropillars,

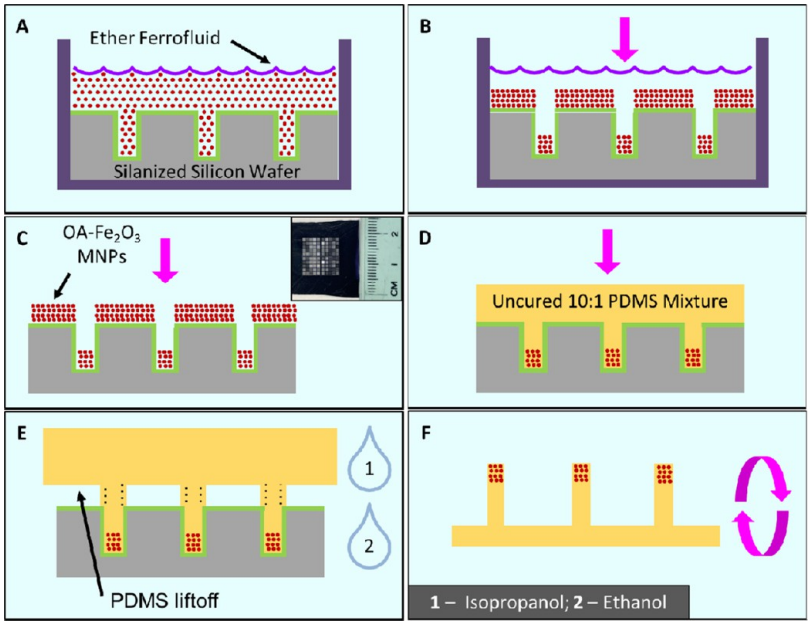

Figure 1. ASAP fabrication protocol. (A) Ether ferrofluid is applied to the surface of an etched and silanized silicon mold confined in a scintillation vial. (B) Vial is centrifuged, allowing magnetic particles to fill the mold holes. (C) Ether is evaporated. The inset shows a fabricated silicon mold beside a ruler for scale. (D) Mold surface is cleaned using silicone tape to remove residual magnetic material, clean PDMS is added and centrifuged to fill mold holes, and then PDMS is cured at 80 °C overnight. (E) Cured ASAP are swollen in isopropanol then deswollen/dried in the 80 °C oven to allow for gentle loosening of surface contact with the mold. Dried PDMS is then submerged in ethanol overnight to fill between the PDMS and silicon surfaces and aid release. (F) ASAP are removed from the mold and left free standing in the ethanol environment. Diagram is not to scale.

which we call actuating surface-attached post (ASAP) arrays. Furthermore, our design process allows a variety of ASAP array designs to be fabricated on a single mold. Our process produces large arrays of high aspect ratio soft structures with submicron cross-sections without the practical limitations associated with electron beam lithography or contact lithography patterning. Other methods can be limited by long fabrication processing times, small feature resolution of the photolithography technique and instrument, and lower aspect ratio in the final mold.

In our prior published work,[16,26−30] we chose to provide an actuating capability for our ASAP with a magnetic actuation system due to its noninvasive nature and the ability to create diverse actuation patterns. Magnetic actuation systems offer a high level of design flexibility and vary in complexity, from a single permanent magnet[1,2,16,21] to multiple electromagnets,[18,31] among other setups.[4,30] To ensure efficient magnetic actuation, attention must be given to the design of the mechanical and magnetic properties of micropillars. Magnetic nanocomposite materials offer process simplicity but can be limited to low concentrations of magnetic material and particle size heterogeneity due to surface energy differences.[32,33] To avoid these issues, we add the magnetic material and silicone elastomer to the mold in separate centrifugal deposition steps, allowing us to achieve uniform thickness in the layer of magnetic material in a high aspect ratio mold. Centrifugation drives material out of suspension and into a compact, concentrated pellet or into a film on a substrate.[15,34−37]

Fabrication of flexible structures like ASAP necessitates the use of elastomeric materials like silicones and hydrogels, but these materials are susceptible to damage during the demolding process. Our fabrication exploits the solvent swelling properties of poly(dimethylsiloxane) (PDMS) as characterized by Lee et al.[38] to gently release our structures from hard molds. PDMS swelling has been exploited to release nonfragile PDMS structures from fragile hard molds.[39] We expand these techniques by utilizing the swelling properties to release small, fragile PDMS structures from hard molds.

The high level of fabrication control provides a platform to test theoretical models, which show that paired reciprocal actuators can skirt the restrictions of the famous "scallop theorem"[40,41] to induce directed flow in a low Re environment. Models predict that actuation phase differences are critical for propelling flow for paired reciprocal actuators. To develop this platform, we created herringbone arrays which consist of rectangular actuators at right angles to each other in close proximity. We designed these arrays to permit independent control over the relative phase of actuation between adjacent rectangular actuators, and we present data demonstrating success.

We also investigate deterministic lateral displacement (DLD) effects that have not been explored. DLD concepts have been used to inform the design of both passive and active micropillar arrays tailored to particle and droplet size separation and filtration.[11,42−47] However, these micropillars are typically cylinders spanning the width of the channel normal to the direction of flow and experiments with such arrays focus on long-term particle separation and filtering. To our knowledge, flow parallel to the boundary between a free channel and a region of posts has not been studied. At the interface between the post array and the open region of the channel, particles are "skimmed" or separated from the open region into the post array. Understanding flow dynamics in this regime will inform design considerations for bulk flow control, "shielding" regions of the microchannel from flow, and particle sorting throughout the microchannel.

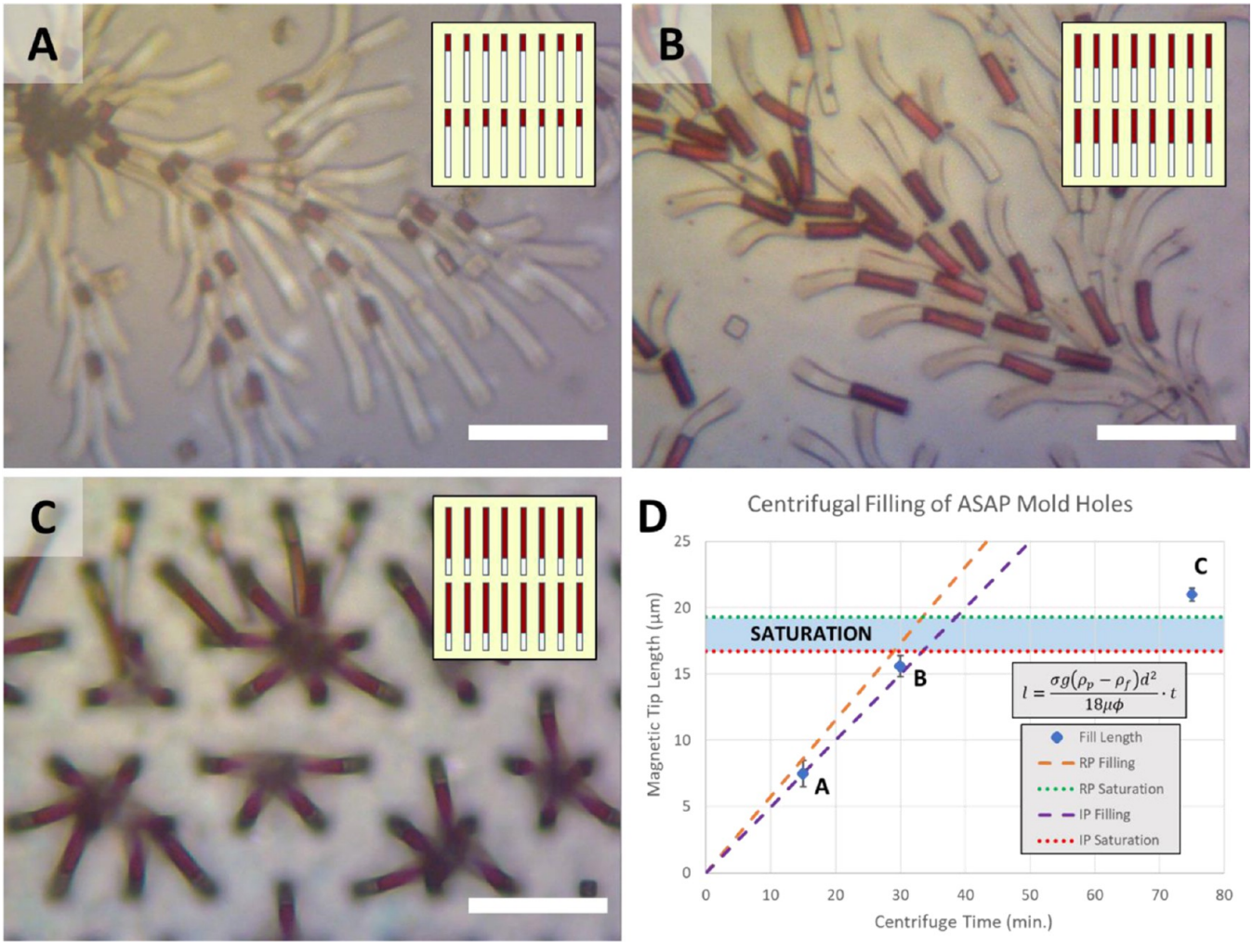

Figure 2. Centrifugal deposition provides predictive magnetic length. Four micrometer square ASAP mold holes are filled with Fe_2O_3 nanoparticles as shown in (A–C), where posts have been intentionally collapsed to facilitate the evaluation of Fe_2O_3 filling. All centrifugation parameters remain unchanged except for centrifugation time as: (A) 15 min, (B) 30 min, and (C) 75 min. (D) Approximate filling length as a function of centrifugation time; the inset shows the linear relationship. Points "A," "B," and "C" refer to the ASAP shown in panels (A–C), respectively. The linear trend continues until the ferrofluid is cleared of nanoparticles in the blue saturation band. Five millimeter layer of ether ferrofluid (0.25% Fe_2O_3 by volume) used in depositions. RP and IP here refer to "random packing" and "ideal packing" ratios of spheres, 0.64 and 0.74, respectively. Theoretical filling curves for RP and IP are defined by the broken orange and purple lines, respectively. Theoretical filling saturation limits for RP and IP are defined by dotted horizontal green and red lines, respectively. Scale bars are 40 μm.

EXPERIMENTAL APPROACH

Our fabrication process is detailed in Figure 1, starting from a silane-treated silicon hard mold carrying 50 unique ASAP array designs. Preceding fabrication steps can be found in the Supporting Information. Following a recipe, we synthesized an aqueous ferrofluid containing maghemite (γ-Fe_2O_3) nanoparticles. We characterized these nanoparticles using transmission electron microscopy (TEM; see Figure S1). We isolated these nanoparticles and suspended them in diethyl ether (see the Supporting Information for more details). The centrifugal deposition was used to fill mold holes with this magnetic material, as shown in Figure 2. The microfluidic device assembly protocol is detailed in Figure 3. Additional details about process steps can be found in the Methods section in the Supporting Information.

An organic ferrofluid suspension expedites evaporation of the carrier fluid after deposition. Nanoparticles were initially treated with oleic acid to prevent flocculation and to keep magnetic nanoparticles suspended in ether. This surface treatment reduces surface energy differences between the particles and PDMS in later fabrication steps. The ether ferrofluid was deposited onto the silane-treated mold, and the sample was then centrifuged. During this process, the ether was evaporated while under centrifugation to prevent loss of magnetic filling through capillary action that we found occurs during static solvent drying (see the Supporting Information for centrifugation parameters). Process parameters were tuned to allow for controllable deposition of magnetic material into the holes of the silicon mold, as seen in Figure 1 and discussed in the Results section. It was crucial to place the mold into the centrifuge on a flat surface to prevent the mold from shifting and cracking and to ensure uniform and successful filling.

After centrifugation with the concomitant ether evaporation, we use a layer of thin silicone adhesive tape to pull the dried material from the silicon surface while leaving nanoparticles in the holes. We then mixed the Sylgard 184 kit (DOW Corning) in a 10:1 ratio of base polymer to curing agent, applied the Sylgard 184 to the mold surface, and centrifuged to fill the high aspect ratio mold holes with the clear silicone. The Sylgard 184 (henceforth referred to as "PDMS") ratio can be modified to modulate the mechanical properties of the cured elastomer. Following the work of Palchesko et al. to modulate PDMS stiffness,[23] we have successfully fabricated ASAP with elastic modulus as low as approximately 250 kPa. This is a key fabrication parameter to optimize because softer silicones are more difficult to demold but have the advantage of offering higher peak deflection in a magnetic field for a given post geometry. After the initial centrifugation cycle, the PDMS

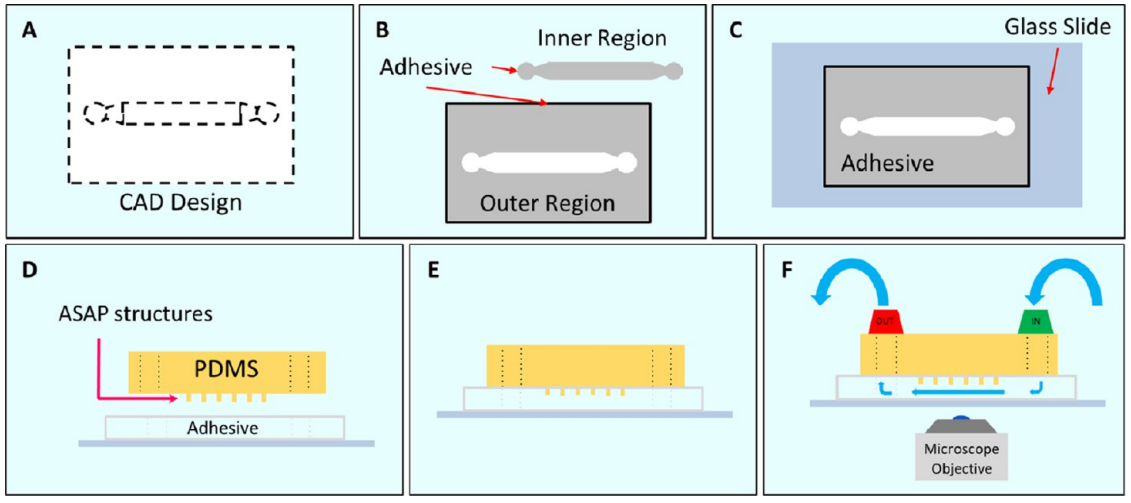

Figure 3. Enclosed channel assembly protocol. CAD design of channel outline (A) defines the laser cut of thin silicone adhesive. (B) Laser cut adhesive sections are separated, and the outer region is retained as the channel body. Adhesive thickness determines the clearance above post tips. (C) Sheet adhesive is sealed to a plasma-cleaned glass slide. (D) Remaining liner is removed, ports are aligned, and ASAP slab is carefully sealed to the adhesive sheet. (E) Sealed device with defined microfluidic channel. (F) Appropriate microfluidic tubing and couplings are added to complete the microfluidic device. Diagram is not to scale.

was degassed in a Fisher Scientific Isotemp Vacuum Oven Model 280A, and the mold was centrifuged a second time. We then cured the PDMS in the Fisher Isotemp oven at 80 °C overnight. The cured ASAP were removed from the oven and allowed to cool. Excess PDMS was carefully cut away, and the cured ASAP structures in the mold (ASAP/mold) were soaked in isopropanol (Fisher Scientific) for 24 h, which swelled the cured PDMS about 9% by volume.[38] This property has not been previously exploited for the gentle release of high aspect ratio elastomeric structures from silicon molds. Once ASAP were swelled to saturation, the excess isopropanol was removed, and the ASAP were dried in the 80 °C oven overnight, which reduced the PDMS to its original volume. The ASAP/mold were submerged in ethanol, and the ASAP were gently separated from the mold with light pressure with forceps. Some posts exhibited ground collapse after complete demolding. Collapsed posts were recovered to their upright position through ultrasonication (see the Supporting Information). When all ASAP were standing, the entire sample was dried using a critical point drier. Solvent swelling caused some temporary structural changes in the PDMS that were reversed with deswelling and critical point drying. Most fluids that are biologically compatible (some applications of ASAP include biological experimentation) have no swelling effect on the PDMS. ASAP in Figure 4 were critical point dried (CPD) before they were characterized with the scanning electron microscope (SEM). In our experience, CPD is beneficial for some surface functionalization techniques and is necessary for mounting ASAP in a microfluidic channel.

The mounting process is shown in Figure 3. We designed a microfluidics channel in TurboCAD and cut the shape in Adhesives Research ARcare 90106 silicone adhesive using a laser cutter. The channel was adhered to a glass slide that had been cleaned with an oxygen plasma in a Harrick Plasma PPC-001 O_2 plasma cleaner. The ASAP were inverted and fixed to the adhesive and secured by gently pressing around the adhesive area to ensure a watertight seal. Microfluidics couplings, tubing, and syringes were then added to complete device fabrication. The completed device was aligned on the microscope and fixed in place. Fluorescent bead solution was pumped through the channel, and the flow was aligned using controlled clamping of the microfluidic input tubes. Once flow was aligned, videos of fluid flow were captured.

RESULTS

Scanning electron microscope (SEM) images of high aspect ratio ASAP fabricated using our protocol are shown in Figure 4. Using the process outlined above, we made PDMS posts with a minimum cross-sectional area of less than 1 square micron with a maximum aspect ratio (AR) of 23:1. Irregularities in post profile along the length of the post reflect irregularities in the silicon mold. As an example, smaller cross-section posts are considerably wider near the base (Figure 4B). This is an artifact of the extended deep reactive ion etching (DRIE) process; lateral etching near the opening of the etch area widens the hole and is visible in the base of the posts. Aside from absolute aspect ratio measurements, we also offer a "minimal AR" and an "actuation AR." Minimal AR is the length of the post measured from the actuation point to the tip divided by the width of the post measured at the widest point of the post along that length. This minimal AR is about 14:1. Actuation AR is the length of the post measured from the actuation point to the tip divided by the width of the post measured at the actuation point. The actuation point is just above the wide portion of the base of the posts visible in Figure 4B. The actuation AR is about 16.5:1. The actuation AR is an important value because it reflects the length of the post that will move under actuation and affects how easily the post can be actuated. The optics of the lithography system affect crispness of sharp cross-section features, like corners, at the micron to submicron feature size we are patterning in the photoresist layer. Figure 4 shows square, rectangular, and herringbone ASAP arrays; all posts in a single-array pattern have a uniform height. Post height changes with post cross-section because of the deep reactive ion etching DRIE process. We have fit 100 total ASAP patterns onto a square silicon mold roughly 12.5 mm on a side (Figure 1C, inset).

The centrifugal deposition process is highlighted in Figure 2. The process can be fine-tuned through modification of various parameters according to the relationships established in eq 1. Our method for incorporating magnetic nanoparticles is simple, and by keeping magnetic nanoparticles separate from the silicone elastomer, we avoid the hassle of creating and characterizing a nanocomposite material. Furthermore, this centrifugal deposition method has intrinsic flexibility in the type of particle deposited on the mold. The method naturally lends itself to controlled loading of other particles such as silica to increase post tip stiffness while retaining a pliable base or

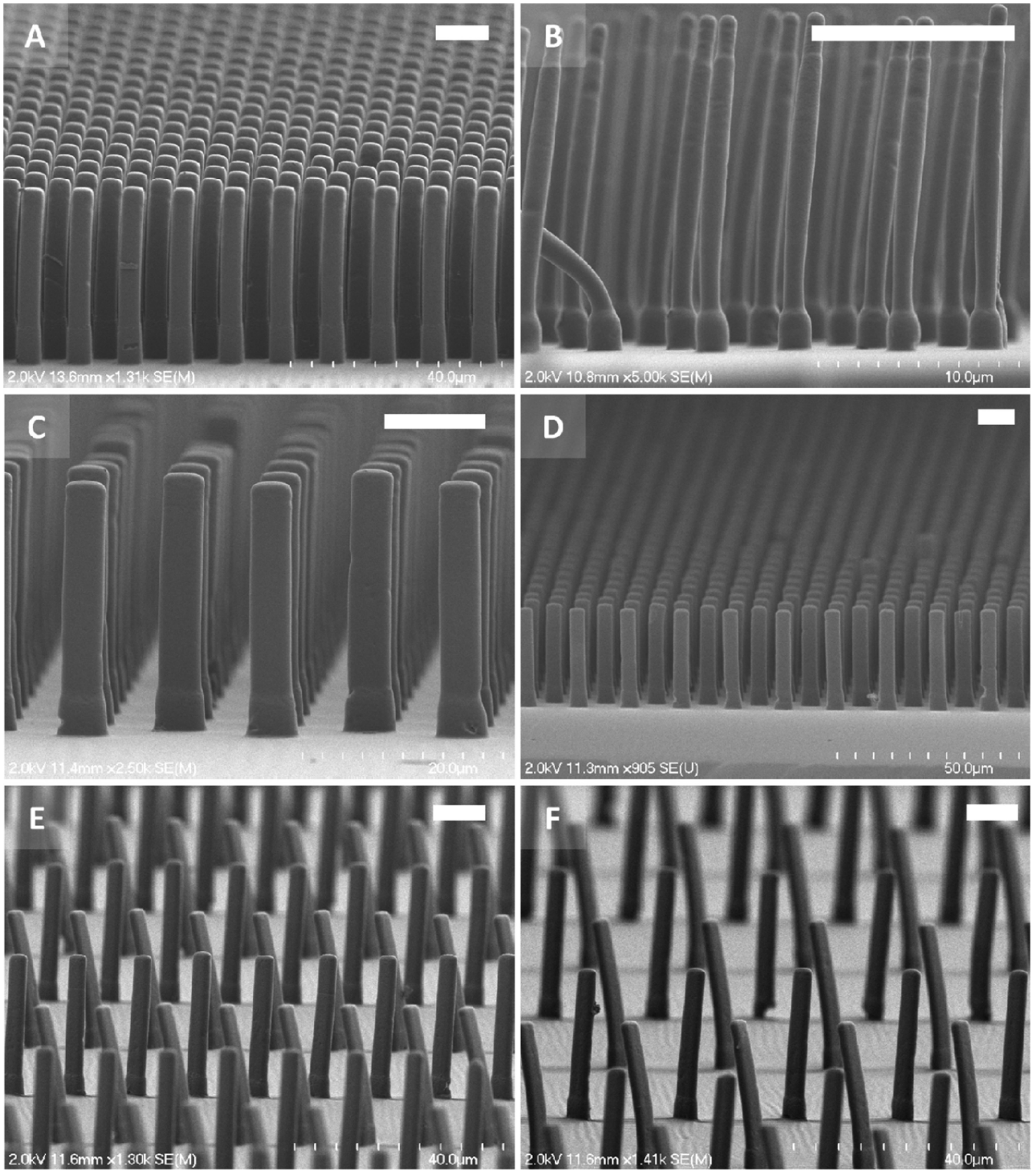

Figure 4. (A, B) Square cross-sectional ASAP (side lengths of 3.85 and 0.72 μm, respectively), with (B) showing ASAP with an aspect ratio 23:1. At smaller sizes, square posts become more cylindrical because of our fabrication process as seen in (B). (C, D) Rectangular cross-section ASAP. (E, F) Herringbone ASAP at two packing densities. Scale bars are 10 μm.

fluorescent nanoparticles so post tips can be visible during fluorescent imaging applications such as those with cells.

Figure 2A–C shows increasing length of the region of magnetic material, visible as brown against the optically clear PDMS. Figure 2D depicts the filling of the magnetic material as a function of centrifuge time. Here, we account for both ideal and random sphere packing ratios (broken purple and orange lines, respectively). For early times, the data are consistent with a linear dependence. At longer times, deposition was limited by the concentration and volume of ferrofluid. The deposition was limited by the complete clearing of magnetic nanoparticles from the ether ferrofluid suspension where the filling had reached

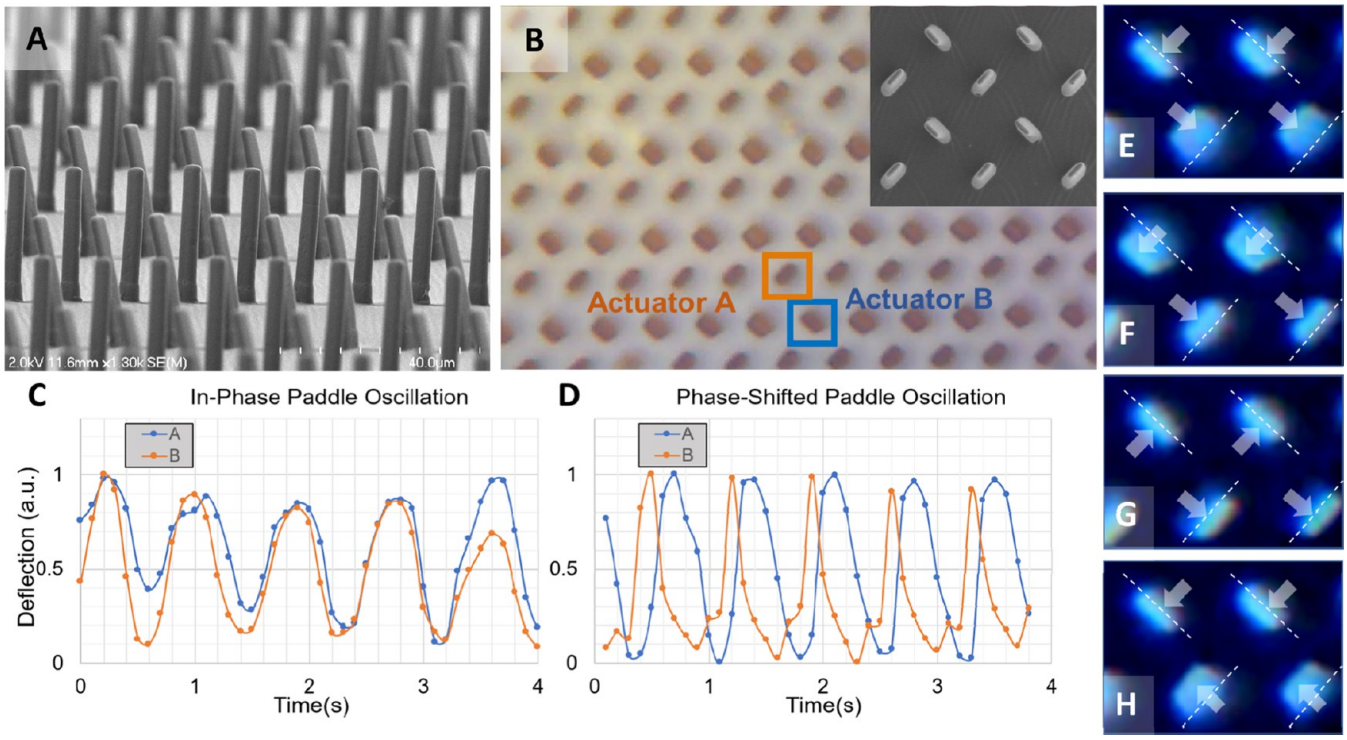

Figure 5. Herringbone arrays provide independent subpopulation actuation. (A) Scanning electron microscopy image of herringbone ASAP. (B) Optical image of array from a video (see Supporting Video 1) of actuating ASAP; the inset shows an SEM image of an alternative array with different post spacing that was also fabricated. (C, D) Herringbone pair (identified in B) in-phase and out-of-phase herringbone ASAP actuation based on analysis of intensity changes. (E–H) Magnified frames from the actuation video. Broken lines indicate rest (nonactuated) positions of posts, and arrows indicate deflection direction in the frame. Video colors were inverted for clarity in the intensity measurements and to highlight the actuation phase difference in (C, D). Scale bars are 10 μm.

saturation. Again, we account for saturation in the case of ideal (IP) and random (RP) sphere packing ratios (dotted red and green lines, respectively). This was governed by the volume and concentration of ferrofluid; we centrifuged a sample with a 5 mm thick layer of ferrofluid at 0.25% Fe_2O_3 volume. The saturation region defined by the horizontal band represents the range of magnetic layer thickness between an IP a RP nanoparticle layer (assuming spherical nanoparticles). The saturation limit can be overcome by simply increasing the starting volume of ferrofluid. However, overfilling is not desired since ASAP that are completely filled with magnetic material will essentially be maghemite rods. These will be difficult to actuate without the PDMS hinge region available. Sample C was centrifuged for 75 min, more than twice the theoretical clearing time of about 33.5 min. This sample showed filling consistent with saturation of the silicon mold with all magnetic material in the volume of ferrofluid at an earlier point in the centrifugation process. Figure 2D shows that the filling deviated from the expected linear behavior at higher spin times because the fluid is fully cleared of nanoparticles at an earlier time. Error bars shown represent the standard deviation of tip length for each sample. Some posts, especially sample C, were not fully collapsed and length measurements are based on the visible projection of the post. Additionally, our theoretical filling calculations assume uniform spherical maghemite nanoparticles. Heterogeneity in particle size and changes in density due to the oleic acid coating can influence fill times. Meng et al. determine the effective density of the oleic acid-coated nanoparticles to be 2.92 g/cm^3 in a similar fabrication process to ours using particles of the same size as ours.[48] An oleic acid molecule is about 1.97 nm in length. We adjusted for these changes in density and particle diameter with the introduction of an oleic acid layer; however, theoretical filling times calculated for OA-Fe_2O_3 magnetic nanoparticles (MNPs) were nearly identical to filling times for bare Fe_2O_3 MNPs. With our control over the addition of magnetic material, we can optimize filling for any cross-section. Optimization is informed by the magnetoelastic ratio[26] and similar characterization metrics. Using these metrics to determine fabrication parameters will allow us to circumvent a full parametric sweep of post aspect ratios, cross-sectional shapes, and magnetic fillings. Mold fabrication time makes it impractical to test a series of ASAP molds with varying ARs.

Deposition dynamics are governed by Stokes drag and buoyancy of a sphere moving in a fluid in a centrifugal force field. These principles guided theoretical calculations for IP and RP filling and saturation. We assume that centrifugation results in uniform deposition of magnetic material such that the length of the magnetic region of the ASAP tips will be equivalent to the thickness of the deposited layer of magnetic material. We varied the length of these magnetic tips by varying centrifugation time to control filling. Equation 1 shows that layer thickness is linearly dependent on centrifugation time

$$l = \frac{\sigma g(\rho_p - \rho_f)d^2}{18\mu\phi}\cdot t = \frac{\sigma\pi^2\zeta^2 r(\rho_p - \rho_f)d^2}{16200\mu\phi}\cdot t \quad (1)$$

Here, l is the thickness of the layer of magnetic material; σ is the volume percent concentration of the ether ferrofluid; t is centrifugation time; g is the acceleration applied by the centrifuge; ρ_p and ρ_f are the mass density of Fe_2O_3 nanoparticles and the ether carrier fluid, respectively; d is the diameter of a

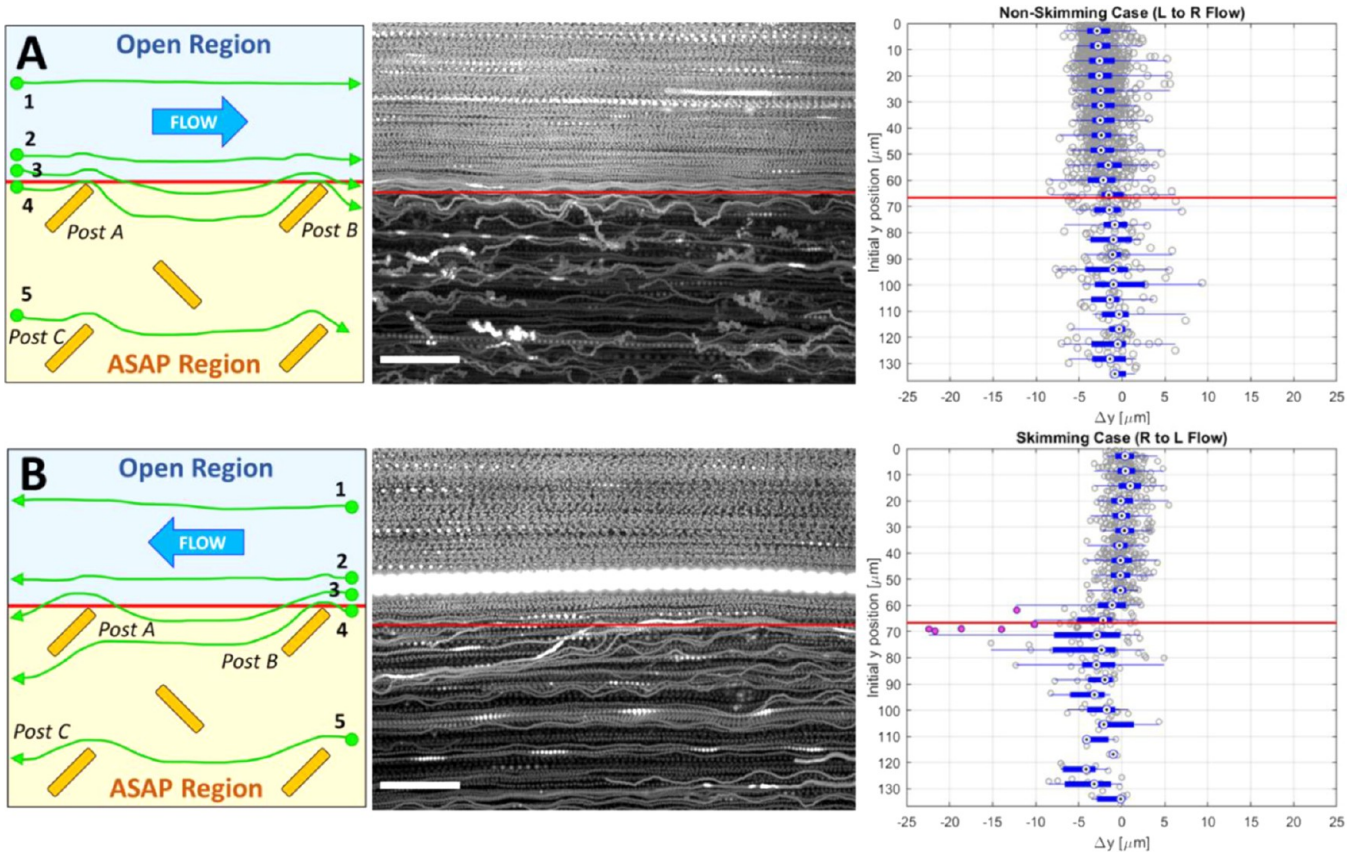

Figure 6. Skimming behavior at the interface of the ASAP and open regions of the microfluidic channel (defined by the red line). (A) Left to right (LTR) bulk flow direction. Tracker paths oscillate along the interface but do not enter the array. (B) Right to left (RTL) bulk flow direction. Trackers near the interface can be skimmed into the array. For (A, B), maximum intensity projections of tracker paths can be seen in the middle column. The rightmost column has box plots overlaid on scatter plots showing how tracker y-position across the path changes (Δy) as a function of initial y-position. Blue boxes are positioned based on y-position and span the interquartile range (25−75%) of trackers with nearby initial y-positions, and the blue whiskers include all trackers with Δy outside the respective interquartile range. While not every tracker in this region will be skimmed, skimming events (designated with pink circles) are only observed in RTL flow for the defined field of view. The cartoon diagrams are a scale representation of the experimental system. Rectangular posts are 5 μm long and 1 μm wide, and the array has a 20 μm center to center spacing between posts A and B, and 12 μm center to center spacing between posts A and C. Scale bars in center panels are 30 μm.

single Fe_2O_3 nanoparticle (13.9 nm, see the Supporting Information); μ is the dynamic viscosity of the carrier fluid, and φ is the sphere packing ratio (0.68 for random packing and 0.74 for ideal packing, denoted as RP and IP respectively in Figure 2D). The equation can also be written in terms of the input spin speed ζ (rpm), and r is the radius of the centrifuge using $g = \pi^2\zeta^2 r/900$.

We created herringbone ASAP (Figure 4E,F) that allow testing of theoretical fluid propulsion models. The herringbone pattern is an array of coupled actuators where adjacent rectangular flaps are positioned perpendicular to one another. We refer to these as "1-dimensional actuators" in the sense that they have a preferred bending direction according to the minimal second moment of inertia of the cross-section. Therefore, to first order, the herringbone ASAP move only along a single axis in the horizontal plane (see Supporting Video 1). In Figure 5, we have shown both in-phase and out-of-phase reciprocal (time symmetric) actuation patterns with herringbone arrays. This indicates that we have independent control of herringbone structures in the same. In Figure S2, we show nonreciprocal (time asymmetric) actuation patterns with the same array pattern. We show control over the relative phase of actuation between neighboring reciprocal actuators, a critical experimental parameter for testing theoretical models of coupled actuators propelling flow. With simple magnetic actuation, we achieved actuation phase differences between adjacent actuators of up to $\pi/2$. We have also achieved selective control of these paired actuators such that actuator A is static while actuator B in motion and vice versa (not shown here). Current herringbone actuators exhibit about 10° of deflection from their static vertical position with reciprocal actuation patterns shown in Figure 5. We have achieved a maximum deflection of 15° from vertical for another post design. All of this was achieved using a simple magnetic actuation system that is described in the Supporting Information. We can increase actuation with changes to our magnetic setup and changes to the mechanical and magnetic properties of the ASAP themselves. In our prior published work, we have characterized a more complex magnetic actuation system and will use this system to create more complex actuation patterns.[29]

We also investigated how passive herringbone ASAP arrays affected pressure-driven flow in regions at the boundary between open-channel flow and the ASAP patterns. We found that herringbone structures caused particles flowing near the border between the ASAP array and open channel to be displaced into the array and to remain in the array. We refer to this displacement as "skimming," and we hypothesize that the frequency of skimming events is determined by the balance of

diffusion and convection at the chosen flow speed. Figure 6 shows how bulk flow direction affects whether particles are skimmed as they flow along the border between the open region and the region populated by ASAP. Figure 6A,B shows diagrams of fluid flow in the region of interest near the ASAP region border with left to right (LTR) and right to left (RTL) flow directions, respectively. Note how bulk flow direction affects the path of tracker 3 in the diagrams. Alongside these diagrams are maximum intensity projections capturing the tracks of fluorescent tracers, which highlight the tracks taken by fluorescent beads through the field of view (FOV). We used every tenth frame of the video to construct the maximum intensity projection, so some tracks appear to be discontinuous in still images. A large, out-of-focus bead clump obscured some of the tracks in the RTL maximum intensity projection; however, this did not affect the tracking of other beads in that region. We analyzed fluorescent bead movement using Video Spot Tracker, a home-built tracking software (cismm.web.unc.edu/software/) and used Matlab to visualize trends in the tracking data. We plotted the initial y-position of a tracker in the FOV against the change in y-position (Δy) of a bead during its lifetime in the video. These scatterplot data were used to construct the overlaid boxplot to clarify the Δy trends at different points in the FOV (details in Figure 6 caption). In our FOV, a negative Δy value corresponds to a tracker moving downward in the FOV, corresponding to movement toward the array side. A tracker was considered "skimmed" if it moved into the array region without later exiting the region. We expected any skimming events to occur with trackers that enter the FOV near the interface between the ASAP region and open region of the channel and that a large negative Δy value would be associated with skimmed trackers.

The herringbone structures at the boundary have an angle relative to bulk flow direction, which we will refer to as "angle of attack." LTR bulk flow in the FOV corresponds to a negative angle of attack, while RTL flow corresponds to a positive angle of attack. For both positive and negative angle of attack, we see small shifts in the open-channel region with higher variability in the ASAP region as expected. However, flow behavior near the border of the post region varies with the angle of attack relative to the bulk flow. With a positive angle of attack, there is a subtle but clear shift in mean Δy value in the negative direction. There is no shift for the negative angle of attack (6A). Skimming events are only present for the right to left flow, and individual trackers that are skimmed are identified by red circles in the scatterplot. Criteria for identifying skimming events can be found in the Supporting Information. As an additional note, there is a visible skew of bulk flow in the open region of the FOV in the left to right flow video that favors a negative Δy. This bias should encourage skimming events to occur, yet we observe none in the left to right flow direction.

CONCLUSIONS

We present a robust method for the fabrication of high aspect ratio magnetically actuatable elastomeric posts. We have demonstrated the fabrication of posts with various designed cross-sectional shapes, with submicron minimum feature size, and with an aspect ratio greater than 20:1 (Figure 4). The centrifugal filling method enabled control over magnetic material independent of other factors like ferrofluid concentration or aggregation of the nanoparticles in the elastomer network. Introducing the elastomer and the magnetic material in separate steps in the process allowed for control over the magnetic filling of the posts while maintaining an optically clear base layer for simple microscopy. The wet release method will be important in future fabrication of ASAP arrays with small area base PDMS, such as ASAP-based microswimmers that are even more fragile than large-area arrays.

Using herringbone arrays, we demonstrated controlled phase differences in beating for adjacent symmetric actuators. In future work, we will use the properties of the actuating herringbone structures to explore theoretical predictions that coupled reciprocal actuators can create fluid transport. We will also expand our actuation capabilities with magnetic systems providing more spatial and temporal flexibility described in prior work.[29]

We also demonstrated particle skimming using passive ASAP arrays. Our herringbone arrays skim particles from the open region of the channel into the post region when the posts have a positive angle of attack relative to the bulk flow direction. Herringbones have inspired us to develop "funnel" and "street" elements in our ASAP arrays that can select flowing particles by size and then "steer" them through the microchannel to a particular destination such as an outlet port for collection and analysis. Modifying the geometric parameters of the array, the viscoelastic properties of the fluid or the flow parameters may amplify or suppress this effect. Future studies will expand on this work by exploring the effect of fluid viscosity, flow speed, bead diameter, and interpost spacing on the frequency of such skimming events. An immediate study of interest is the effect of flow velocity and magnetic post actuation on interfacial skimming behavior in the fluid flow.

ASSOCIATED CONTENT

Supporting Information

The Supporting Information is available free of charge at https://pubs.acs.org/doi/10.1021/acsapm.1c01133.

TEM micrograph of bare Fe_2O_3 magnetic nanoparticles (Figure S1); nonreciprocal actuation of herringbone ASAP (Figure S2); field of view at the interface between herringbone posts and the open channel (Figure S3); fluorescent trackers skimmed by herringbone array- (Figure S4); silicon mold fabrication; Fe_2O_3 organic ferrofluid fabrication; sample characterization; ultrasonic recovery; centrifugal filling parameters; herringbone actuation analysis; passive asap data collection; identification of skimming events; and magnetic actuation system (PDF)

ASAP_herringbone_actuation (AVI)

AUTHOR INFORMATION

Corresponding Authors

Jacob T. Brooks − *Department of Physics & Astronomy, The University of North Carolina, Chapel Hill, North Carolina 27599, United States;* orcid.org/0000-0001-5526-0107; Email: brooksjt@live.unc.edu

Richard Superfine − *Department of Applied Physical Sciences, The University of North Carolina, Chapel Hill, North Carolina 27599, United States*; Email: superfine@unc.edu

Authors

Jeremy Cribb − *Department of Physics & Astronomy, The University of North Carolina, Chapel Hill, North Carolina 27599, United States*

Michael R. Falvo − *Department of Physics & Astronomy, The University of North Carolina, Chapel Hill, North Carolina 27599, United States*

Complete contact information is available at: https://pubs.acs.org/10.1021/acsapm.1c01133

Funding

J.T.B., J.C., M.R.F., and R.S. received funding from the National Institutes of Health (NIBIB 5-P41-EB002025). J.T.B., M.R.F., and R.S. received funding from the National Science Foundation (CEBT-2114078). This work was performed in part at the NCSU Nanofabrication Facility (NNF), a member of the North Carolina Research Triangle Nanotechnology Network (RTNN), which is supported by the National Science Foundation (Grant ECCS-1542015) as part of the National Nanotechnology Coordinated Infrastructure (NNCI). This work was performed in part at the Chapel Hill Analytical and Nanofabrication Laboratory, CHANL, a member of the North Carolina Research Triangle Nanotechnology Network, RTNN, which is supported by the National Science Foundation, Grant ECCS-1542015, as part of the National Nanotechnology Coordinated Infrastructure, NNCI.

Notes

The authors declare the following competing financial interest(s): Richard Superfine and Michael Falvo have equity stake in, and Richard Superfine is the Executive Chairman of Redbud Labs, Inc, which has license to the ASAP technology evaluated in this study. This does not alter our adherence to ACS Applied Polymer Materials policies on sharing data and materials.

REFERENCES

(1) Ben, S.; Zhou, T.; Ma, H.; Yao, J.; Ning, Y.; Tian, D.; Liu, K.; Jiang, L. Multifunctional Magnetocontrollable Superwettable-Microcilia Surface for Directional Droplet Manipulation. *Adv. Sci.* **2019**, *6*, No. 1900834.

(2) Wang, Z.; Wang, K.; Liang, D.; Yan, L.; Ni, K.; Huang, H.; Li, B.; Guo, Z.; Wang, J.; Ma, X.; Tang, X.; Chen, L. Q. Hybrid Magnetic Micropillar Arrays for Programmable Actuation. *Adv. Mater.* **2020**, *32*, No. 2001879.

(3) Dwiyantoro, B. A.; Chau, S. W. The influence of cross-sectional shape and orientation of micropillar surface on microdroplet formation by a dewetting process. *J. Eng. Technol. Sci.* **2013**, *45*, 166−178.

(4) Zhang, S.; Zuo, P.; Wang, Y.; Onck, P.; den Toonder, J. M. J. Anti-Biofouling and Self-Cleaning Surfaces Featured with Magnetic Artificial Cilia. *ACS Appl. Mater. Interfaces* **2020**, *12*, 27726−27736.

(5) Zhang, X.; Guo, J.; Fu, X.; Zhang, D.; Zhao, Y. Tailoring Flexible Arrays for Artificial Cilia Actuators. *Adv. Intell. Syst.* **2021**, No. 2000225.

(6) Fisher, J. T.; Gurney, T. O.; Mason, B. M.; Fisher, J. K.; Kelly, W. J. Mixing and oxygen transfer characteristics of a microplate bioreactor with surface-attached microposts. *Biotechnol. J.* **2021**, *16*, No. e2000257.

(7) Zhu, S.; Eldeeb, M. A.; Pang, S. W. 3D nanoplasmonic biosensor for detection of filopodia in cells. *Lab Chip* **2020**, *20*, 2188−2196.

(8) Kajzar, A.; Cesa, C. M.; Kirchgeßner, N.; Hoffmann, B.; Merkel, R. Toward physiological conditions for cell analyses: Forces of heart muscle cells suspended between elastic micropillars. *Biophys. J.* **2008**, *94*, 1854−1866.

(9) Yang, Z.; Park, J. K.; Kim, S. Magnetically Responsive Elastomer−Silicon Hybrid Surfaces for Fluid and Light Manipulation. *Small* **2018**, *14*, No. 1702839.

(10) Guo, D.-J.; Liu, R.; Cheng, Y.; Zhang, H.; Zhou, L.-M.; Fang, S.-M.; Elliot, W. H.; Tan, W. Reverse Adhesion of a Gecko-Inspired Synthetic Adhesive Switched by an Ion-Exchange Polymer−Metal Composite Actuator. *ACS Appl. Mater. Interfaces* **2015**, *7*, 5480−5487.

(11) Salafi, T.; Zhang, Y.; Zhang, Y. A Review on Deterministic Lateral Displacement for Particle Separation and Detection. *Nano-Micro Lett.* **2019**, *11*, No. 77.

(12) McGrath, J.; Jimenez, M.; Bridle, H. Deterministic lateral displacement for particle separation: A review. *Lab Chip* **2014**, *14*, 4139−4158.

(13) Du, S.; Drazer, G. Gravity driven deterministic lateral displacement for suspended particles in a 3D obstacle array. *Sci. Rep.* **2016**, *6*, No. 31428.

(14) Yan, T. Particle trajectories around solid or fluid obstacle in microfluidic channels 2016.

(15) Chai, Z.; Liu, M.; Chen, L.; Peng, Z.; Chen, S. Controllable directional deformation of micro-pillars actuated by a magnetic field. *Soft Matter* **2019**, *15*, 8879−8885.

(16) Evans, B. A.; Shields, A. R.; Carroll, R. L.; Washburn, S.; Falvo, M. R.; Superfine, R. Magnetically actuated nanorod arrays as biomimetic cilia. *Nano Lett.* **2007**, *7*, 1428−1434.

(17) Jeon, J.; Park, J. E.; Park, S. J.; Won, S.; Zhao, H.; Kim, S.; Shim, B. S.; Urbas, A.; Hart, A. J.; Ku, Z.; Wie, J. J. Shape-Programmed Fabrication and Actuation of Magnetically Active Micropost Arrays. *ACS Appl. Mater. Interfaces* **2020**, *12*, 17113−17120.

(18) Jiang, W.; Wang, L.; Ye, G.; Chen, B.; Yin, L.; Shi, Y.; Liu, H. Biomimetic magnetic-responsive cilia-like soft device: surface energy control and external field actuation. *J. Mater. Sci.: Mater. Electron.* **2019**, *30*, 3767−3772.

(19) Li, Q.; Dhakal, R.; Kim, J. Microdroplet-based On-Demand Drawing of High Aspect-Ratio Elastomeric Micropillar and Its Contact Sensing Application. *Sci. Rep.* **2017**, *7*, No. 17009.

(20) Luo, Z.; Zhang, X. A.; Chang, C. H. Magnetically responsive polymer nanopillars with nickel cap. *Nanotechnology* **2021**, *32*, No. 205301.

(21) Luo, Z.; Zhang, X. A.; Evans, B. A.; Chang, C. H. Active Periodic Magnetic Nanostructures with High Aspect Ratio and Ultrahigh Pillar Density. *ACS Appl. Mater. Interfaces* **2020**, *12*, 11135−11143.

(22) Paek, J.; Kim, J. Microsphere-assisted fabrication of high aspect-ratio elastomeric micropillars and waveguides. *Nat. Commun.* **2014**, *5*, No. 3324.

(23) Palchesko, R. N.; Zhang, L.; Sun, Y.; Feinberg, A. W. Development of polydimethylsiloxane substrates with tunable elastic modulus to study cell mechanobiology in muscle and nerve. *PLoS One* **2012**, *7*, No. e51499.

(24) Zhang, S.; Cui, Z.; Wang, Y.; den Toonder, J. M. J. Metachronal actuation of microscopic magnetic artificial cilia generates strong microfluidic pumping. *Lab Chip* **2020**, *20*, 3569−3581.

(25) Zhang, S.; Wang, Y.; Onck, P. R.; den Toonder, J. M. J. Removal of Microparticles by Ciliated Surfaces—an Experimental Study. *Adv. Funct. Mater.* **2019**, *29*, No. 1806434.

(26) Evans, B. A.; Fiser, B. L.; Prins, W. J.; Rapp, D. J.; Shields, A. R.; Glass, D. R.; Superfine, R. A Highly Tunable Silicone-Based Magnetic Elastomer with Nanoscale Homogeneity. *J. Magn. Magn. Mater.* **2012**, *324*, 501−507.

(27) Evans, B. A.; Superfine, R. Design Considerations for Magnetically Actuated Biomimetic Cilia. In *Biomimetic Based Applications*; Anne, G., Ed.; InTech: Rijeka, Croatia, 2011.

(28) Fiser, B. L.; Shields, A. R.; Falvo, M. R.; Superfine, R. Highly responsive core-shell microactuator arrays for use in viscous and viscoelastic fluids. *J. Micromech. Microeng.* **2015**, *25*, No. 025004.

(29) Judith, R. M.; Lanham, B.; Falvo, M. R.; Superfine, R. Microfluidic viscometry using magnetically actuated micropost arrays. *PLoS One* **2018**, *13*, No. e0200345.

(30) Shields, A. R.; Fiser, B. L.; Evans, B. A.; Falvo, M. R.; Washburn, S.; Superfine, R. Biomimetic cilia arrays generate simultaneous pumping and mixing regimes. *Proc. Natl. Acad. Sci. U.S.A.* **2010**, *107*, 15670−15675.

(31) Gu, H.; Boehler, Q.; Cui, H.; Secchi, E.; Savorana, G.; De Marco, C.; Gervasoni, S.; Peyron, Q.; Huang, T. Y.; Pane, S.; Hirt, A. M.; Ahmed, D.; Nelson, B. J. Magnetic cilia carpets with programmable metachronal waves. *Nat. Commun.* **2020**, *11*, No. 2637.

(32) Shrestha, S.; Wang, B.; Dutta, P. Nanoparticle processing: Understanding and controlling aggregation. *Adv. Colloid Interface Sci.* **2020**, *279*, No. 102162.
(33) Zhu, N.; Ji, H.; Yu, P.; Niu, J.; Farooq, M. U.; Akram, M. W.; Udego, I. O.; Li, H.; Niu, X. Surface modification of magnetic iron oxide nanoparticles. *Nanomaterials* **2018**, *8*, No. 810.
(34) Markelonis, A. R.; Wang, J. S.; Ullrich, B.; Wai, C. M.; Brown, G. J. Nanoparticle film deposition using a simple and fast centrifuge sedimentation method. *Appl. Nanosci.* **2015**, *5*, 457−468.
(35) Lu, Z.; Owens, H. Optimum processing parameters for coating polyester with silica nanoparticles using gravity sedimentation. *J. Nanopart. Res.* **2019**, *21*, No. 212.
(36) South, A. B.; Whitmire, R. E.; García, A. J.; Lyon, L. A. Centrifugal Deposition of Microgels for the Rapid Assembly of Nonfouling Thin Films. *ACS Appl. Mater. Interfaces* **2009**, *1*, 2747−2754.
(37) Gaysornkaew, S.; Tsumori, F. Active control of surface profile by magnetic micropillar arrays. *Jpn. J. Appl. Phys.* **2021**, *60*, No. SCCL02.
(38) Lee, J. N.; Park, C.; Whitesides, G. M. Solvent Compatibility of Poly(dimethylsiloxane)-Based Microfluidic Devices. *Anal. Chem.* **2003**, *75*, 6544−6554.
(39) Jiang, Y.; Parameswaran, R.; Li, X.; Carvalho-de-Souza, J. L.; Gao, X.; Meng, L.; Bezanilla, F.; Shepherd, G. M. G.; Tian, B. Nongenetic optical neuromodulation with silicon-based materials. *Nat. Protoc.* **2019**, *14*, 1339−1376.
(40) Purcell, E. M. Life at Low Reynolds Number. *Am. J. Phys.* **1977**, *45*, 3−11.
(41) Lauga, E. Life around the scallop theorem. *Soft Matter* **2011**, *7*, 3060−3065.
(42) Beech, J. P.; Keim, K.; Ho, B. D.; Guiducci, C.; Tegenfeldt, J. O. Active Posts in Deterministic Lateral Displacement Devices. *Adv. Mater. Technol.* **2019**, *4*, No. 1900339.
(43) Cui, H.-h.; Lim, K.-M. Micro-pillar barriers for guiding, mixing, and sorting droplets. In *Transducers*; Denver: CO, USA, 2009; pp 817−820.
(44) Kim, S. C.; Wunsch, B. H.; Hu, H.; Smith, J. T.; Austin, R. H.; Stolovitzky, G. Broken flow symmetry explains the dynamics of small particles in deterministic lateral displacement arrays. *Proc. Natl. Acad. Sci. U.S.A.* **2017**, *114*, E5034−E5041.
(45) Li, Y.; Zhang, H.; Li, Y.; Li, X.; Wu, J.; Qian, S.; Li, F. Dynamic control of particle separation in deterministic lateral displacement separator with viscoelastic fluids. *Sci. Rep.* **2018**, *8*, No. 3618.
(46) Pariset, E.; Berthier, J.; Pudda, C.; Navarro, F.; Icard, B.; Agache, V. Particle Separation with Deterministic Lateral Displacement (DLD): The Anisotropy Effect. *Proceedings* **2017**, *1*, No. 313.
(47) Xavier, M.; Holm, S. H.; Beech, J. P.; Spencer, D.; Tegenfeldt, J. O.; Oreffo, R. O. C.; Morgan, H. Label-free enrichment of primary human skeletal progenitor cells using deterministic lateral displacement. *Lab Chip* **2019**, *19*, 513−523.
(48) Meng, X.; He, Z.; Zhao, J.; Lin, Y.; Liu, X.; Li, D.; Li, J.; Qiu, X. Oleic Acid Surface Modification in the Preparation of Magnetic Nanoparticles by a Chemically Induced Transition. *IEEE Trans. Magn.* **2018**, *54*, 1−7.